Journal of Alloys and Compounds 506 (2010) 231–236

Contents lists available at ScienceDirect

Journal of Alloys and Compounds

journal homepage: www.elsevier.com/locate/jallcom

Influence of Li addition on charge/discharge behavior of spinel lithium titanate

Chien-Te Hsieh[a,b,*], Jia-Yi Lin[a]

[a] Department of Chemical Engineering and Materials Science, Yuan Ze University, Taoyuan 320, Taiwan
[b] Yuan Ze Fuel Cell Center, Yuan Ze University, Taoyuan 320, Taiwan

ARTICLE INFO

Article history:
Received 4 March 2010
Received in revised form 24 June 2010
Accepted 30 June 2010
Available online 7 July 2010

Keywords:
Li-ion battery
Anode
Spinel structure
Lithium titanate
Rate capability

ABSTRACT

This article provides proof of an efficient approach to adjust the behavior of Li^+ intercalation into $Li_4Ti_5O_{12}$ spinel structures prepared by spray-drying followed by solid-state calcination. The spherical $Li_4Ti_5O_{12}$ powders consist of a number of grains with an average size of 300–500 nm, showing high rate capability at various rates of 0.1–20 C. The addition of Li-ions greatly modifies the $Li_4Ti_5O_{12}$ crystallites with different relative intensity ratios of (3 1 1)/(4 0 0), R value, determined from X-ray diffraction results. The overall reversible capacity in the voltage range of 2.5–0.01 V vs. Li/Li^+ is limited by the vacant tetrahedral (8a) and octahedral (16c) sites. The decrease of capacity ratio of second plateau (1.0–0.01 V) to first plateau (2.5–1.0 V) with the R value proves that the ratio of site vacancy greatly affects the capacity contribution. At high C rates, the tetrahedral (8a) sites exhibit a better accessibility to accommodate Li-ions during the intercalation process, compared with the accessibility of octahedral (16c) sites. This extra capacity of $Li_4Ti_5O_{12}$, originating from the Li^+ insertion at low potential, facilitates not only an enhanced reversible capacity but also a wider working voltage, leading to a higher energy density for rechargeable Li-ion batteries.

1. Introduction

Spinel-type lithium titanate ($Li_4Ti_5O_{12}$) is very promising as an oxide anode electrode material in high-power lithium-ion batteries and in hybrid supercapacitors [1–4]. It has shown a Li-ion insertion and extraction reversibility and good structural stability with zero-strain during the charge/discharge processes [3,5,6], inducing longer cycle life and better safety compared with carbon materials. This material accommodates Li-ions with a theoretical capacity of 175 mAh g^{-1} with excellent cyclability and displays a mid-discharge platform approximating 1.55 V vs. Li/Li^+ [4,7–9]. In most studies, $Li_4Ti_5O_{12}$ powders or thin films have been successfully synthesized using solid-state reaction [10,11], electrostatic spray deposition [12], ball-milling [13,14], sol–gel method [9,15], spray-drying/pyrolysis [1,4,7,16,17], and colloid templated method [18]. The as-grown $Li_4Ti_5O_{12}$ products exhibited specific energy density as high as the theoretical capacity in the voltage range of 2.5–1.0 V vs. Li/Li^+, demonstrating active hosts for the Li^+ intercalation and de-intercalation. Traditionally, solid-state reaction is one of the commonly used methods in synthesizing $Li_4Ti_5O_{12}$ powders in several micron meters. Recently, several groups have devoted to preparing nanocrystalline $Li_4Ti_5O_{12}$, using aqueous combustion process with amino akanine [19], cellulose-assisted glycine-nitrate combustion [20], and ball-milling-assisted sol–gel method [21]. This achievement directs us into the synthesis of nanocrystalline $Li_4Ti_5O_{12}$ with high rate capability.

It is generally recognized that the theoretical capacity of $Li_4Ti_5O_{12}$ is defined by its crystal structure, i.e., spinel structure with $Fd3m$ space group [4,22,23], as shown in Fig. 1. From the conventional viewpoint, the capacity of spinel $Li_4Ti_5O_{12}$ is limited by the number of available octahedral sites, i.e., (16c) sites, to accommodate Li-ions [24]. Recently, the Li-ion insertion has been considered to be three crystallographic sites, i.e., the (8a), (16c), and (48f) sites [3,23], indicating the possibility that Li-ions intercalate into $Li_4Ti_5O_{12}$ at low potential (<1.0 V vs. Li/Li^+). This low-potential intercalation process would lead to improvement of the energy density of spinel $Li_4Ti_5O_{12}$ electrodes, relating to the numbers of octahedral (16c) and tetrahedral (8a) sites and their occupancies. Few reports, however, focus on the intercalation and de-intercalation of Li-ions at low potential and study the influence of site occupancies on the performance of $Li_4Ti_5O_{12}$ anodes.

To examine intercalation behavior at low potential, this study investigates the site occupancy affecting the charge/discharge performance by using different Li/Ti atomic ratios in spinel

---

* Corresponding author at: Department of Chemical Engineering and Materials Science, Yuan Ze University, 135, Yuan-Tung Rd., Chung-Li, Taoyuan 320, Taiwan. Tel.: +886 3 4638800x2577, fax: +886 3 4559373.
E-mail address: cthsieh@saturn.yzu.edu.tw (C.-T. Hsieh).

0925-8388/$ – see front matter © 2010 Elsevier B.V. All rights reserved.
doi:10.1016/j.jallcom.2010.06.183

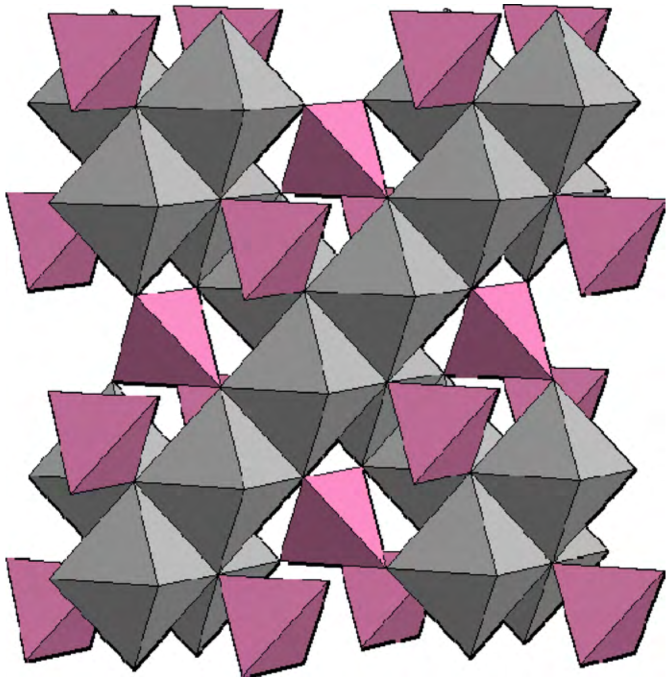

Fig. 1. Crystal structures of spinel $Li_4Ti_5O_{12}$. Pink tetrahedra represent (8a) sites, gray octahedra represent (16c) sites.

$Li_4Ti_5O_{12}$ crystals. Spherical-type $Li_4Ti_5O_{12}$ anode powders were first synthesized by spray-drying followed by solid-state reaction. A post-treatment, using the additive of LiOH followed by thermal treatment, was applied to tune the ratio of (16c) to (8a) site numbers in the spinal crystalline structure, resulting in various charge/discharge platforms. This fundamental research should shed some light on (i) how the occupied sites modify Li^+ insertion/de-insertion behavior and (ii) the low-potential intercalation for preparing spinel $Li_4Ti_5O_{12}$ with a higher energy density.

2. Experimental

Spherical $Li_4Ti_5O_{12}$ powders were synthesized by spray-drying precursor slurries of LiOH and anatase TiO_2 nanoparticles, followed by solid-state calcination. The precursor slurry consisted of LiOH, TiO_2, surface surfactant, and distilled water. The molar ratio of lithium to titanium was set at 4:5. Here a commercial TiO_2 nanopowder (P25, Degussa Co.) with an average size of 20–40 nm served as the precursor material. The slurry with ZrO_2 balls was well mixed by a 3D rotary mixer at a speed of 300 rpm for 4 h. After that, the well-dispersed slurry was atomized at 250 °C using a two-fluid nozzle with an atomizing pressure of $4\,kg\,cm^{-2}$. A homemade tank was used to collect the spray-dried precursor powders for further solid-state calcination. Prior to calcination, the precursors were impregnated in three concentrations of LiOH solution (i.e., 0.1, 0.3, and 0.5 M) with a fixed ratio of 1:20 in w/v ($g\,L^{-1}$) at room temperature for 8 h. The Li^+-adsorbed precursors were calcined at 850 °C under an air atmosphere for 12 h, giving spinel $Li_4Ti_5O_{12}$ powders. The calcination temperature selected in this study depended on our preliminary study, e.g., incomplete transformation of precursor at 800 °C and grain agglomeration at 900 °C. The as-prepared $Li_4Ti_5O_{12}$ samples were designated as sample L, sample M, and sample H, corresponding to different LiOH concentrations of 0.1, 0.3, and 0.5 M, respectively.

The structural observation of $Li_4Ti_5O_{12}$ powders was carried out by using field-emission scanning electron microscopy (FE-SEM; JEOL 2010F) and high-resolution transmission electron microscope (HR-TEM; JEOL, JEM-2100). The crystalline structure of $Li_4Ti_5O_{12}$ samples was characterized by X-ray diffraction (XRD) with Cu Kα radiation, using an automated X-ray diffractometer (Shimazu Labx XRD-6000).

The electrochemical measurements of $Li_4Ti_5O_{12}$ powders were done by coin cell testing platform. Prior to the formation of electrodes for electrochemical tests, each $Li_4Ti_5O_{12}$ anode material was added into a solution of poly-vinylidenefluoride (PVdF) in N-methyl pyrrolidinone (NMP), and the mixture was mixed at ambient temperature to form an electrode slurry. The mixtures were blended by a 3D mixer using zirconia balls for 3 h to prepare uniform slurries. All electrodes were prepared by pressing the slurry on copper foils with a doctor blade, followed by evaporating the solvent, NMP, with a blow dryer. The electrode layers, which consisted of 82 wt.% $Li_4Ti_5O_{12}$ active material, 10 wt.% PVdF binder, 4 wt.% Super-P (Taiwan Maxwave Co., Ltd.), and 4 wt.% KS-6 (Taiwan Maxwave Co., Ltd.) conductive agent, were adjusted to have a thickness of 100 μm. In the test cells, lithium metal and porous polypropylene film served as counter electrode and separator, respectively. The electrolyte solution was 1.0 M $LiPF_6$ in a mixture of ethylene carbonate, polycarbonate, and dimethyl carbonate with a weight ratio of 3:2:5. The charge/discharge cycling test at various *C* rates (from 0.1 to 20 C) was performed within the voltage region of 0.01–2.5 V vs. Li/Li^+ at room temperature.

3. Results and discussion

Fig. 2(a) and (b) shows FE-SEM images of the precursors prepared by spray-drying process with low and high magnifications, respectively. The images clearly show that each precursor had spherical shape with an average diameter of 4–6 μm. The precursor powders were made from a large amount of TiO_2 nanoparticles having a size of 20–40 nm, and thus exhibited a porous nanostructure. The morphology design therefore incorporated nanosized primary grains into micrometer-sized secondary particles, providing good grain-grain contacts and adequate particle size. Such a unique particle would benefit the *C*-rate capability due to its shorter diffusion pathways. Fig. 2(c)–(f) shows FE-SEM images of $Li_4Ti_5O_{12}$ particles calcined at 850 °C for 12 h with high and low magnifications. After calcination, the powder morphology significantly transformed from porous to dense structure. It can be seen that an obvious growth of grain is associated with the densification of the $Li_4Ti_5O_{12}$ precursors, which has been reported elsewhere [4]. Basically, all calcined $Li_4Ti_5O_{12}$ powders (samples L, M, and H) maintained spherical shape, which consisted of a number of grains. The grains were found to have an increased size of approximately 300–500 nm. The $Li_4Ti_5O_{12}$ particles were generally uniform, leading to a narrow size distribution. This result also indicates that the spherical-like $Li_4Ti_5O_{12}$, prepared by spray-drying followed by solid reaction, improves energy density per electrode area due to the closely packed $Li_4Ti_5O_{12}$ arrangement.

HR-TEM micrographs on as-synthesized $Li_4Ti_5O_{12}$ powder and single grain are illustrated in Fig. 3(a) and (b), respectively. The micrograph apparently confirms the following: (i) the spherical $Li_4Ti_5O_{12}$ consists of a number of primary grains, and (ii) each primary grain has an average size of 300–400 nm. The observation is in agreement with the FE-SEM analysis. A selected-area diffraction (SAD) was applied to analyze the crystalline $Li_4Ti_5O_{12}$ grain, as shown in the inset of Fig. 3(a). The typical SAD image introduces each spot that corresponds to the facet in spinel crystal, indicating the single crystalline pattern of spinel $Li_4Ti_5O_{12}$. To assess the influence of the Li/Ti atomic ratio, the chemical composition of as-grown powders was examined using an inductively coupled plasma-atomic emission spectrometer (ICP-AES). The atomic Li/Ti ratios of samples L, M, and H, determined by the ICP-AES analysis, were 4.09/5, 4.12/5, and 4.16/5, respectively.

The XRD pattern of spray-dried precursor powder shows no peaks of crystal structure of $Li_4Ti_5O_{12}$, as may be seen in Fig. 4. The pattern clearly reflects the appearance of crystalline TiO_2, corresponding to anatase and rutile crystals. Fig. 4 also illustrates typical XRD patterns of calcined $Li_4Ti_5O_{12}$ powders with different concentrations of LiOH additives, i.e., sample H, sample M, and sample L. The peaks at 2θ angles of 18.3°, 35.6°, 43.2°, 57.2°, and 62.9° are indexed as the (1 1 1), (3 1 1), (4 0 0), (4 3.2), (3 3 3), and (4 4 0) reflections of $Li_4Ti_5O_{12}$, respectively. Accordingly, all samples display a single phase with cubic spinel structure and *Fd*3*m* space group (JCPDS card no. 26-1198) [4,14,16]. Very weak peaks observed at 25.3° and 27.4° reflect that the resulting $Li_4Ti_5O_{12}$ particles contain trace amounts of TiO_2, originated from the original TiO_2 precursor. The influence of LiOH additive on the transformation of spinel structures seems to be negligible. It is worth noting, however, that the relative intensity ratio of (3 1 1)/(4 0 0) obviously varies with the concentration of additive. The intensity ratio is defined as *R* value, which has an order as follows: 0.583 (sample

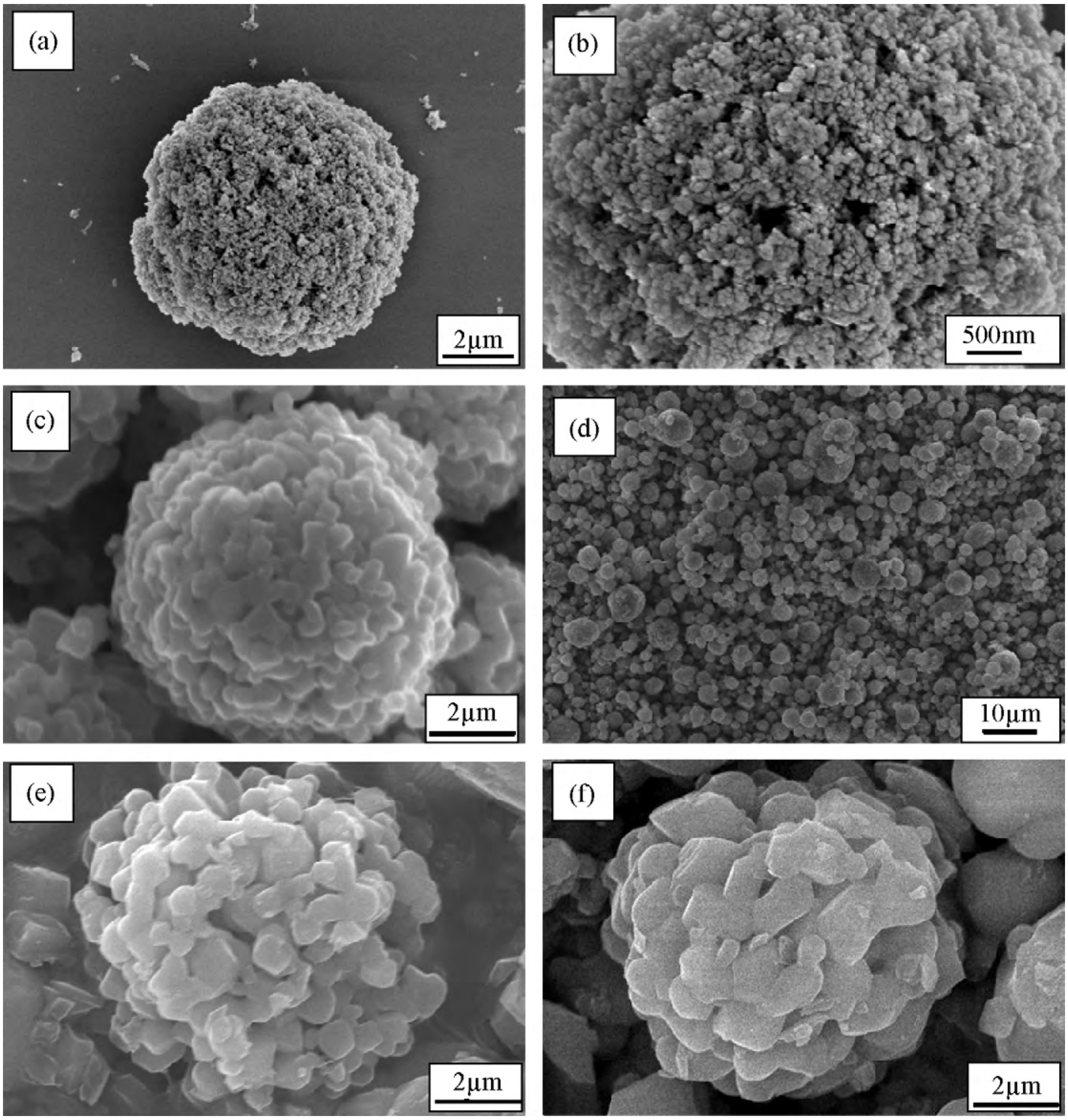

Fig. 2. FE-SEM photographs of spray-dried precursor powders with (a) low and (b) high magnifications. FE-SEM photographs of sintered $Li_4Ti_5O_{12}$ powders (sample L) with (c) low and (d) high magnifications, showing uniform spherical particles consisting of a number of nanosized grains. FE-SEM photographs of sintered $Li_4Ti_5O_{12}$ powders with high magnifications: (e) sample M and (f) sample H.

H) < 0.664 (sample M) < 0.672 (sample L). This result was presumably due to partial sites having been occupied by the Li additive through an inner diffusion during the solid-state calcination. It is generally recognized that the location of Li-ions at tetrahedral (8a) sites or octahedral (16c) sites reflects upon the XRD intensities in the crystalline structures especially for the (3 1 1) and (4 0 0) lines [24]. Based on this result, the Li-ion additives significantly modify the site occupancy for Li-insertion. This means that the additional Li-ions tend to occupy some part of octahedral sites, thus inducing various *R* values for the spinel structures.

The variation of *R* ratio with the Li additive can be explained as follows. Basically, the tetrahedral and octahedral geometries possess the coordination numbers of 4 and 6, respectively, corresponding to cation-anion radius ratios as follows: 0.225–0.414 (tetrahedral) and 0.414–0.732 (octahedral) [25]. This means that the octahedral sites have vacancy with larger size, accessible for the Li^+ occupancy. Thus, when calcination was performed at 850 °C, Li species easily migrated from precursor surface and resided in octahedral sites during the solid-state reaction. From the viewpoint of diffusion kinetics, the diffusion at octahedral sites has a lower energy barrier, i.e., low activation energy, than that at tetrahedral sites. This may be one of the main reasons additional Li-ions tend to occupy some octahedral sites, inducing various *R* values.

Fig. 5(a)–(c) shows typical charge/discharge curves of $Li_4Ti_5O_{12}$ electrodes, samples L, M, and H, respectively, at a constant charge rate of 0.2 C and a discharge rate varied from 0.1 to 20 C at ambient temperature. The charge-discharge cycling was performed within the voltage region between 0.01 and 2.5 V vs. Li/Li^+. The charge process of both electrodes could be divided into three stages: a rapid voltage drop (2.5–1.5 V vs. Li/Li^+), a first plateau (~1.5 V vs. Li/Li^+), and a second plateau (0.8–0.5 V vs. Li/Li^+). The discharge capacities at 0.2 C for all electrodes exceeded 200 mAh g^{-1}, and their capacities were found to decrease with the current density. However, the $Li_4Ti_5O_{12}$ electrodes still maintained a reversible capacity at high *C* rate, e.g., sample L: 108.2 mAh g^{-1} at 20 C. This high *C*-rate capability can be attributed to the fact that the unique nano/microstructure improves the Li-ion diffusion resistance and electron transport.

Interestingly, there were two plateaus during the charge process for all electrodes, but the capacity ratio of first stage (i.e., 2.5–1.0 V vs. Li/Li^+) to second stage (i.e., 1.0–0.01 V vs. Li/Li^+) was obviously found to alter with the *R* value, as determined from

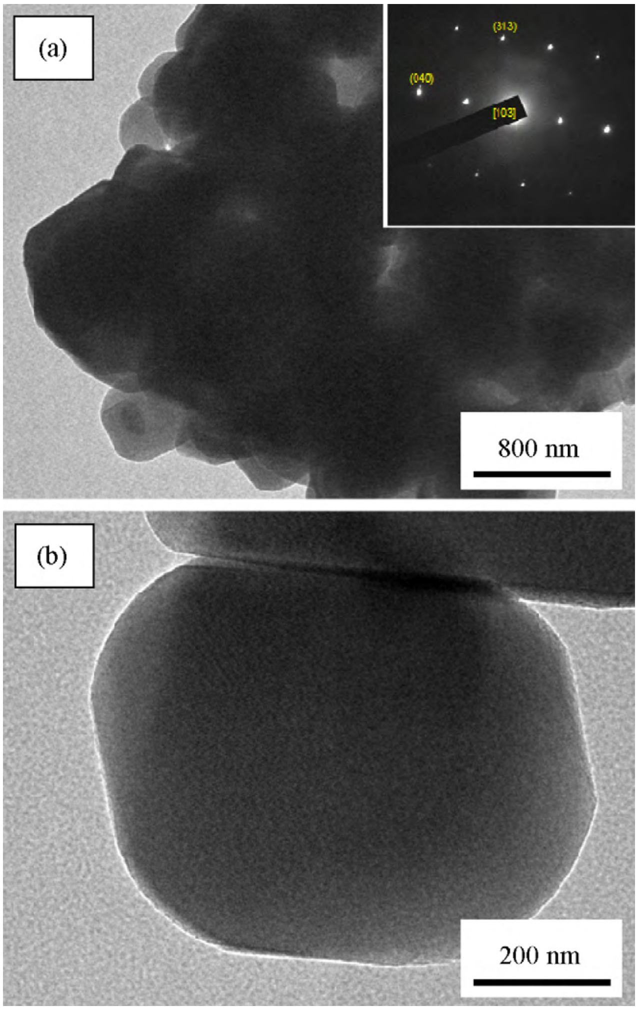

Fig. 3. HR-TEM images of (a) sintered $Li_4Ti_5O_{12}$ powders and (b) single $Li_4Ti_5O_{12}$ grain. The inset is SAD pattern of single grain.

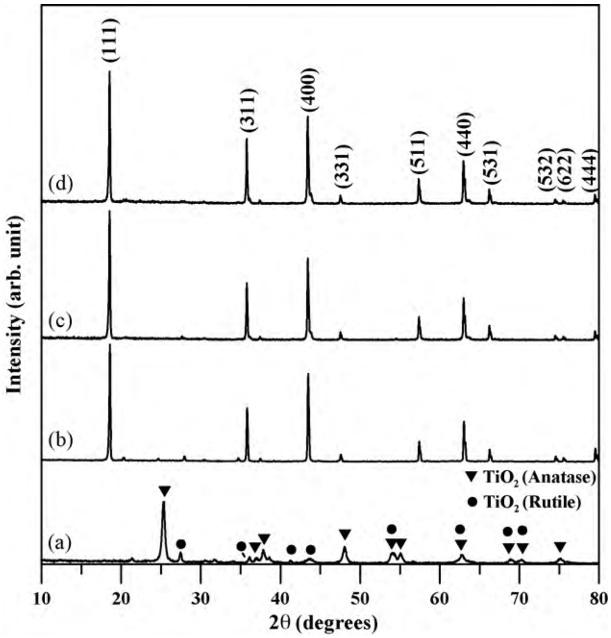

Fig. 4. Typical XRD patterns of (a) spray-dried precursor and calcined $Li_4Ti_5O_{12}$ powders: (b) sample L, (c) sample M, and (d) sample H.

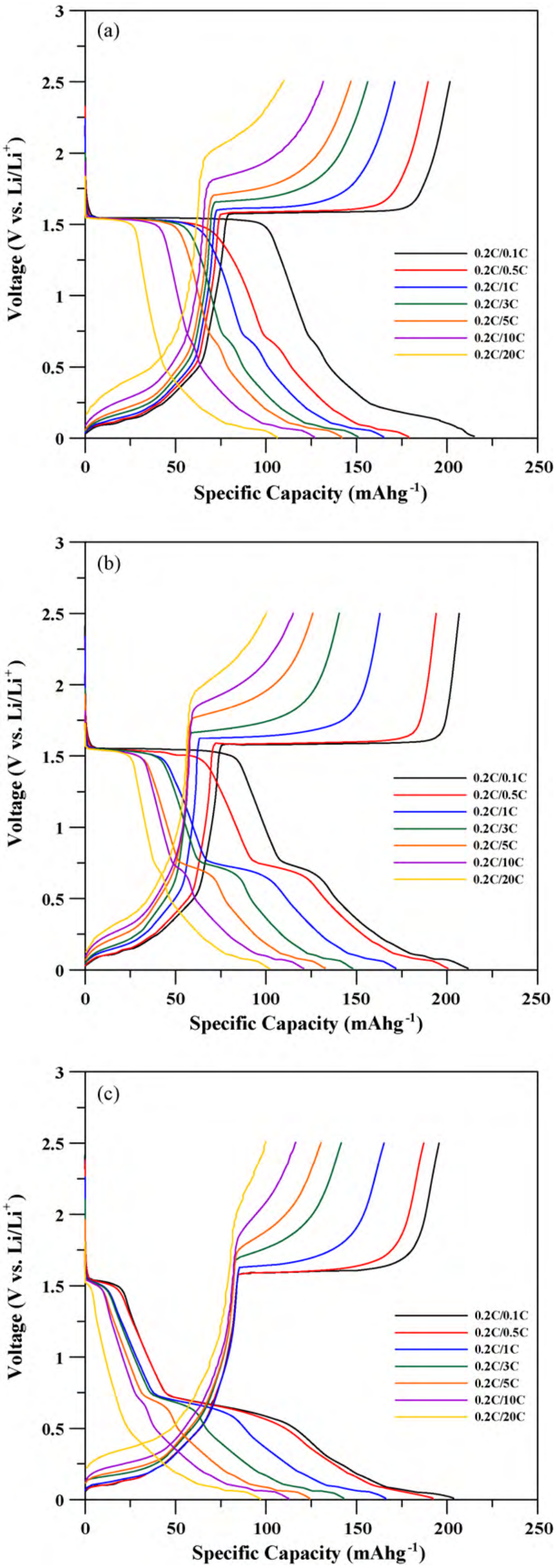

Fig. 5. Typical charge/discharge curves of $Li_4Ti_5O_{12}$ electrodes fabricated with (a) sample L, (b) sample M, and (c) sample H at a constant charge rate of 0.2 C and a discharge rate varied from 0.1 C to 20 C at ambient temperature.

XRD pattern. The reversible charge/discharge curves reveal a possibility that $Li_4Ti_5O_{12}$ electrodes work in a full voltage range between 2.5 and 0.01 V vs. Li/Li^+. Generally, additional Li-ions can be inserted into the lattice and located at octahedral sites in the intercalation process. Meanwhile, lithium ions initially located at tetrahedral sites also transport to octahedral sites. The intercalation/de-intercalation process can thus be expressed as [11,14,17,24]:

$$Li_{3(8a)}[LiTi_5{}^{4+}]_{(16d)}O_{12(32e)} + 3e^- + 3Li^+ \leftrightarrow Li_{6(16c)}[LiTi_3{}^{3+}Ti_2{}^{4+}]_{(16d)}O_{12(32e)} \quad (1)$$

The above reversible reaction takes place in the voltage range of 2.5–1.0 V vs. Li/Li^+, and 3 mol Li-ions are capable of inserting into the octahedral (16c) sites of $Li_4Ti_5O_{12}$ lattices, forming a rocksalt structure [16]. Theoretically, the $Li_4Ti_5O_{12}$ anode offers a reversible capacity of 175 mAh g^{-1}, based on the insertion/de-insertion mechanism in the voltage range of 2.5–1.0 V vs. Li/Li^+. However, the electrode fabricated with sample H exhibits the lowest capacity within the voltage region of 2.5–1.0 V vs. Li/Li^+ since its plateau at 1.5 V almost disappears, as shown in Fig. 5(c). This plateau disappearance becomes more apparent especially for high *C*-rate charging behavior. This result can be ascribed to the fact that a number of octahedral (16c) sites were occupied by excessive Li-ions due to the addition of LiOH during solid-state reaction. Accordingly, this proves the significance of the occupancy of the (16c) and (8a) sites in spinel $Li_4Ti_5O_{12}$ lattice.

To gain further insight into ionic intercalation/de-intercalation at the second stage (i.e., 1.0–0.01 V vs. Li/Li^+), the low-potential charge/discharge process should be carefully examined. A previous study had pointed out that other 2 mol Li-ions could be intercalated into $Li_7Ti_5O_{12}$ if there were enough interstitial sites in $Li_7Ti_5O_{12}$ [24]. The insertion/de-insertion at low potential can be illustrated as

$$\begin{aligned} &Li_{6(16c)}[LiTi_3{}^{3+}Ti_2{}^{4+}]_{(16d)}O_{12(32e)} + 2e^- \\ &\quad + 2Li^+ \leftrightarrow Li_{2(8a)}Li_{6(16c)}[LiTi_5{}^{3+}]_{(16d)}O_{12(32e)} \quad (2) \end{aligned}$$

Here, vacant tetrahedral (8c) sites are available to accommodate Li-ions under 1.0 V vs. Li/Li^+, thus enhancing a reversible capacity at low potential. Accordingly, the second stage of charging plateau contributes to a significant portion of total capacity of $Li_4Ti_5O_{12}$ anodes. Among these $Li_4Ti_5O_{12}$ anodes, the electrodes fabricated with sample L display the highest reversible capacity of ~215.1 mAh g^{-1} within 2.5–0.01 V vs. Li/Li^+ at 0.2 C, which is much higher than the theoretical capacity of 175 mAh g^{-1}. This additional capacity of $Li_4Ti_5O_{12}$, originating from the charge/discharge at low potential, facilitates not only an enhanced reversible capacity but also a wider working voltage, leading to a higher energy density for rechargeable Li-ion batteries.

The role of site number in the charge/discharge behavior of $Li_4Ti_5O_{12}$ anodes was investigated next. The value of *R*, determined from the intensity ratio of (3 1 1) to (4 0 0) peaks, can be an indicator to evaluate the number of tetrahedral (8a) and octahedral (16c) sites. Therefore, before the Li^+ insertion, a smaller *R* value means that the spinel lattice leaves a larger amount of tetrahedral (8a) vacancies accessible for the Li^+ intercalation. On the other hand, a larger *R* value indicates a higher portion of vacant octahedral (16c) sites. Fig. 6 shows the variation of capacity charged within 2.5–1.0 V and 1.0–0.01 V vs. Li/Li^+ with the *R* value. The capacity charged within 2.5–1.0 V is an increasing function of the *R* value, whereas the capacity charged within 1.0–0.01 V shows a decrease with the *R* value. This result indicates that the lower the *R* value, the more tetrahedral (8a) interstitials, which benefits the capacity at low potential (1.0–0.01 V vs. Li/Li^+), i.e., reaction (2). For example, the electrode fabricated with sample H offers ~87% capacity (i.e., 195.6 mAh g^{-1}) from the contribution of tetrahedral (8a) interstitials.

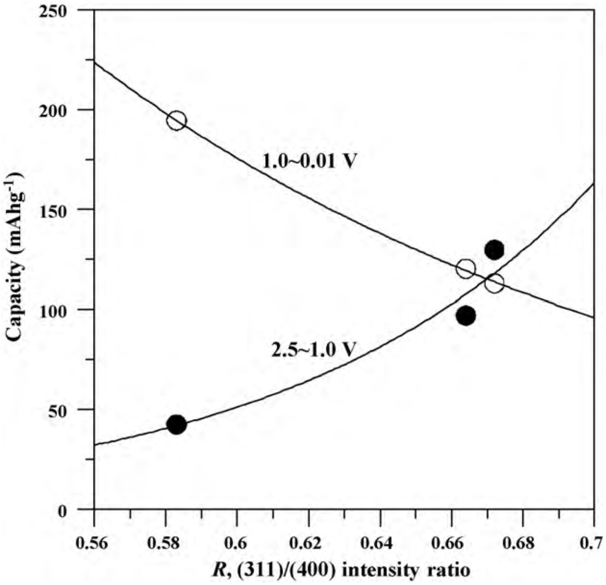

Fig. 6. The variation of capacity charged within 2.5–1.0 V and 1.0–0.01 V vs. Li/Li^+ with the *R* value.

Fig. 7 depicts the plot of capacity ratio of low (1.0–0.01 V) to high (2.5–1.0 V) potential vs. the *R* value. It is reasonable to state that the capacity ratio greatly decreases with the *R* value, indicating that the ratio of vacancy strongly affects the capacity contribution. On the basis of the result, the number of site vacancies would be considered an important factor affecting the Li-insertion behavior of $Li_4Ti_5O_{12}$ anodes. Fig. 7 also clearly shows the relationships between the capacity ratio and the *R* value at different *C* rates. As expected, with increasing *C* rate, all capacity ratios display a decreasing trend, showing the Li^+ diffusion-limited process. The capacity ratio at high *C* rate is comparable with that at low rate, revealing different decline rates. That is, the capacity ratio becomes more evident at high *C* rate, e.g., the ratio ~25.0 at 10 C. This result reflects that all $Li_4Ti_5O_{12}$ anodes show a better rate capability at low potential against the *C* rate. Moreover, a poor rate capability at high potential for all anodes can be observed. It can be inferred

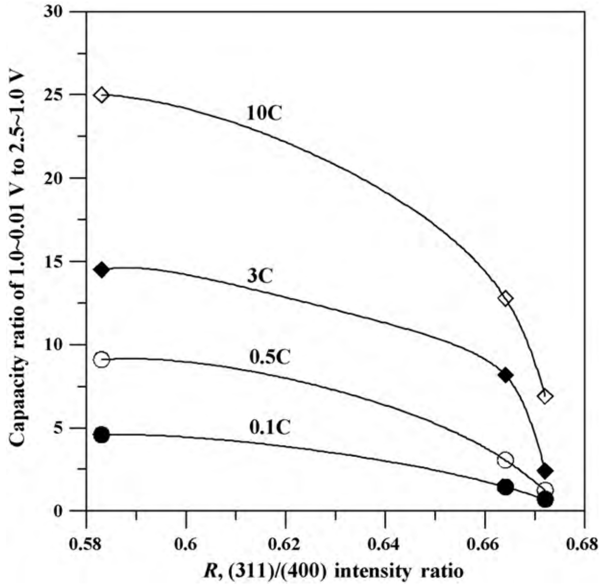

Fig. 7. The variation of capacity ratio of high (2.5–1.0 V) to low potential (1.0–0.01 V) vs. the *R* value at different *C* rates.

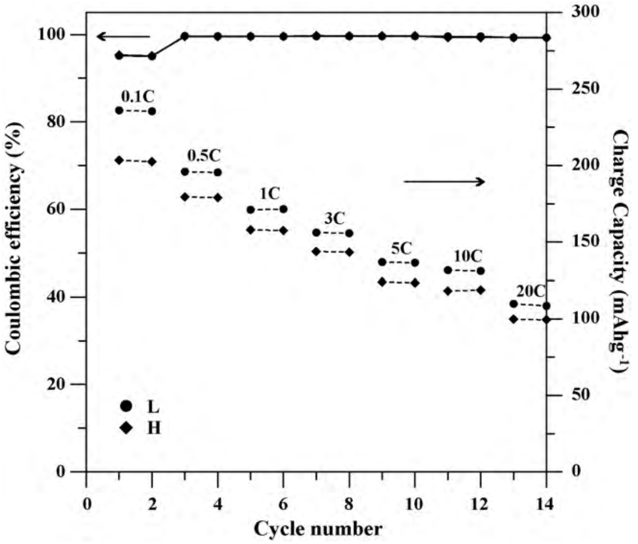

Fig. 8. The charge/discharge cycling tests for two electrodes fabricated with sample H and L at various *C* rates.

from this finding that lithium ions have a better accessibility to insert the tetrahedral (8a) sites during the intercalation process. That is, tetrahedral (8a) sites can be easily occupied by lithium ions. This phenomenon can be briefly described as follows: the two types of sites in the spinel structure are like two baseball catchers, who must precisely catch the ball (Li-ion) thrown by the pitcher (cathode, such as $LiFePO_4$). However, the tetrahedral (8a) site is a good player who is capable of catching slow and fast balls (i.e., at both low and high *C* rates), while octahedral (16c) sites only catch slow balls (i.e., at low *C* rate). Thus, the design of spinel $Li_4Ti_5O_{12}$ anode materials, adjusted by Li/Ti atomic ratio, shows promising potential for high-power Li-ion battery applications.

The charge/discharge cycling tests for two electrodes fabricated with samples H and L at various *C* rates are shown in Fig. 8. It can be seen that all electrodes maintain stable capacities at different *C* rates. The Coulombic efficiencies also show a high value >99.5% during 14 cycles, indicating an excellent reversibility of Li-insertion/de-insertion. The result of cycling stability demonstrates that such design of $Li_4Ti_5O_{12}$ structure presents the feasibility for effective anode materials in the field of energy storage. However, future work still requires a deeper investigation on full cell performance and stability.

4. Conclusions

This study investigated the influence of vacancy number of tetrahedral (8a) and octahedral (16c) sites on the charge/discharge behavior of spinel $Li_4Ti_5O_{12}$ anodes within the entire voltage region of 2.5–0.01 V vs. Li/Li^+. Spherical $Li_4Ti_5O_{12}$ powders were successfully synthesized by spray-drying followed by solid-state calcination. The addition of Li-ions greatly modified the crystalline $Li_4Ti_5O_{12}$ with different relative intensity ratios of (3 1 1)/(4 0 0), *R* value, determined from XRD results. The *R* value was found to influence the charge behavior at low (1.0–0.01 V) and high potential (2.5–1.0 V), confirming that the low- and high-potential reversible capacities are limited by the vacant tetrahedral (8a) and octahedral (16c) sites. The decrease of capacity ratio of second plateau (1.0–0.01 V) to first plateau (2.5–1.0 V) with the *R* value reflected that the ratio of vacancy strongly affects the capacity contribution. The electrodes fabricated with sample L display the highest reversible capacity of ~202 mAh g^{-1} within 2.5–0.01 V vs. Li/Li^+ at 0.1 C. At high *C* rates, the tetrahedral (8a) sites offer better accessibility than do octahedral (16c) sites in accommodating Li-ions during the intercalation process. Accordingly, the site occupancy can be considered a crucial index in evaluating the number of Li-insertion in spinel structure, thus tuning the charge/discharge behavior of $Li_4Ti_5O_{12}$ anodes. This extra capacity of $Li_4Ti_5O_{12}$, originating from the charge/discharge at low potential, promotes not only an enhanced reversible capacity but also a wider working voltage, leading to a higher energy density for rechargeable Li-ion batteries. On the basis of the above deduction, such design of $Li_4Ti_5O_{12}$ structure presents the feasibility for effective anode materials in the field of energy storage.

Acknowledgement

The authors gratefully acknowledge financial support from the National Science Council (NSC) in Taiwan, through Project NSC 98-2120-M-155-001.

References

[1] T. Doi, Y. Iriyama, T. Abe, Z. Ogumi, Chem. Mater. 17 (2005) 1580.
[2] S.C. Lee, S.M. Lee, J.W. Lee, J.B. Lee, S.M. Lee, S.S. Han, H.C. Lee, H.J. Kim, J. Phys. Chem. C 113 (2009) 18420.
[3] K. Kataoka, Y. Takahashi, N. Kijima, H. Hayakawa, J. Akimoto, K. Ohshima, Solid State Ionics 180 (2009) 631.
[4] K.C. Hsiao, S.C. Liao, J.M. Chen, Electrochim. Acta 53 (2008) 7242.
[5] M. Wagemaker, E.R.H. van Eck, A.P.M. Kentgens, F.M. Mulder, J. Phys. Chem. B 113 (2009) 224.
[6] P. Reale, S. Panero, F. Ronci, V. Rossi Albertini, B. Scrosati, Chem. Mater. 15 (2003) 3437.
[7] Z. Wen, Z. Gu, S. Huang, J. Yang, Z. Lin, O. Yamamoto, J. Power Sources 146 (2005) 670.
[8] S. Huang, Z. Wen, B. Lin, J. Han, X. Xu, J. Alloys Compd. 457 (2008) 400.
[9] Y. Hao, Q. Lai, Z. Xu, X. Liu, X. Ji, Solid State Ionics 176 (2005) 1201.
[10] G.J. Wang, J. Gao, L.J. Fu, N.H. Zhao, Y.P. Wu, T. Takamura, J. Power Sources 174 (2007) 1109.
[11] X.L. Yao, S. Xie, H.Q. Nian, C.H. Chen, J. Alloys Compd. 465 (2008) 375.
[12] Y. Yu, J.L. Shui, C.H. Chen, Solid State Commun. 135 (2005) 485.
[13] G. Wang, J. Xu, M. Wen, R. Cai, R. Ran, Z. Shao, Solid State Ionics 179 (2008) 946.
[14] E. Matsui, Y. Abe, M. Senna, A. Guerfi, K. Zaghib, J. Am. Ceram. Soc. 91 (2008) 1522.
[15] N.A. Alias, M.Z. Kufian, L.P. Teo, S.R. Majid, A.K. Arof, J. Alloys Compd. 486 (2009) 645.
[16] S.H. Ju, Y.C. Kang, J. Phys. Chem. Solids 70 (2009) 40.
[17] D. Yoshikawa, Y. Kadoma, J.M. Kim, K. Ui, N. Kumagai, N. Kitamura, Y. Idemoto, Electrochim. Acta 55 (2010) 1872.
[18] E.M. Sorensen, S.J. Barry, H.K. Jung, J.R. Rondinelli, J.T. Vaughey, K.R. Poeppelmeier, Chem. Mater. 18 (2006) 482.
[19] M.W. Raja, S. Mahanty, M. Kundu, R.N. Basu, J. Alloys Compd. 468 (2009) 258.
[20] T. Yuan, K. Wang, R. Cai, R. Ran, Z.P. Shao, J. Alloys Compd. 477 (2009) 665.
[21] G.F. Yan, H.S. Fang, H.J. Zhao, G.S. Li, Y. Yang, L.P. Li, J. Alloys Compd. 470 (2009) 544.
[22] F. Ronci, P. Reale, B. Scrosati, S. Panero, V. Rossi Albertini, P. Perfetti, M. di Nichiel, J.M. Merino, J. Phys. Chem. B 106 (2002) 3082.
[23] L. Aldon, P. Kubiak, M. Womes, T.C. Jumas, J. Olivier-Fourcade, J.L. Tirado, J.I. Corredor, C. Pérez Vicente, Chem. Mater. 16 (2004) 5721.
[24] H. Ge, N. Li, D. Li, C.S. Dai, D.L. Wang, J. Phys. Chem. C 113 (2009) 6324.
[25] W.D. Callister Jr., Fundamentals of Materials Science and Engineering, 2nd ed., John Wiley & Sons, 2005, p. 41.